Unbroken Perovskite: Interplay of Morphology, Electro-optical Properties, and Ionic Movement

Juan-Pablo Correa-Baena, Miguel Anaya, Gabriel Lozano, Wolfgang Tress, Konrad Domanski, Michael Saliba, Taisuke Matsui, Tor Jesper Jacobsson, Mauricio E. Calvo, Antonio Abate, Michael Grätzel, Hernán Míguez,* and Anders Hagfeldt**

Perovskite solar cells (PSCs) composed of organic-metal-halide materials have made impressive progress in just a few years with maximum power conversion efficiencies (PCEs) jumping from 3.8%[1] in 2009 to a certified 21%[2] in 2015. Even though further improvements are still expected, such rapid progress is unprecedented for any photovoltaic material.[2] The general formula of the commonly used perovskite is ABX_3, containing an organic cation A, such as methylammonium (MA) or formamidinium (FA),[1,3] a divalent metal B, such as Pb or Sn,[4] and a halide X, such as bromine or iodine. Perovskite materials can be processed by a large number of techniques ranging from spin coating,[5] dip coating,[6] 2-step interdiffusion,[7] to thermal evaporation.[8,9] The impressive performances achieved to date have been attributed to exceptional material properties such as low charge recombination, high light absorption over the visible spectrum, and charge carrier diffusion lengths in the micrometer range.[10–12]

The combination of a thin TiO_2 mesoporous layer and mixture of halides and cations (referred to in this work as "mixed perovskite") with a precursor composition $FA_{0.83}MA_{0.17}Pb(I_{0.83}Br_{0.17})_3$ has shown to yield the highest PCEs over 20%.[13–15] The key to high performance of these devices is the thick perovskite layer formed atop the thin mesoporous TiO_2 layer, otherwise known as the capping layer, which absorbs most of the photons and effectively separates charges. A few works have varied the perovskite layer thickness and studied their optical properties and influence in photovoltaic parameters.[16,17] A few other studies have focused on understanding the properties of perovskite crystals with respect to their size. Indeed, optical[18,19] and electrical properties have been found to be dramatically affected by the size of these crystals.[20] Nevertheless, to date there exists no comprehensive study of the relation between the perovskite crystal dimensions and the electro-optical properties of record devices, which is imperative to rationalize the origin of both highest efficiencies and the commonly observed current–voltage (*J–V*) hysteresis behavior.

The issue of hysteresis complicates the way efficiency is measured in devices because, depending on prebiasing, scan rate, or scan direction, performance parameters change dramatically. We have shown before that scan rate affects the *J–V* curves, especially the forward scan (from short-circuit, J_{SC}, to open-circuit, V_{OC}), and attributed this to ionic movement in the perovskite layer.[21] In addition, other studies have found that morphology also affects the dynamics of hysteresis.[20] Therefore, further understanding of hysteresis is needed in order to achieve high efficiency devices with long-term stability.

By varying the thickness of the perovskite capping layer, we investigate both its effect on the photocurrent to achieve record photovoltaic characteristics and on the crystal formation, which in turn is found to be responsible for the hysteresis behavior. Perovskite capping layers with a thickness of ≈500 nm are able to absorb most of the light according to the optical model presented here. It was found that crystals of at least 150 nm are required to achieve high fill factor (FF) and hysteresis-free devices. In particular, we demonstrate that thinner layers, composed of small crystals, show high series resistance and slower current transient behavior due to a change in ionic displacement behavior, yielding low FF and highly hysteretic current–voltage curves. On the other hand, faster transient behavior and lower series resistance were demonstrated for larger crystals, which show hysteresis-free *J–V* curves with high photovoltaic parameters and PCEs up to 20.8%.

We prepared PSCs composed of a typical stack of mesoporous-TiO_2/mixed perovskite/Spiro-OMeTAD/gold as presented in **Figure 1**. The perovskite capping layer thickness was modified from 40 to 480 nm as depicted in Figure 1a,b, respectively, and pictures of the full devices can be seen in Figure S1 (Supporting Information). Here the compact TiO_2 and thin mesoporous TiO_2 layers are used as the electron selective layer (ESL),

Dr. J.-P. Correa-Baena, Dr. T. J. Jacobsson, Prof. A. Hagfeldt
Laboratory of Photomolecular Science
Institute of Chemical Sciences and Engineering
École Polytechnique Fédérale de Lausanne
1015 Lausanne, Switzerland
E-mail: juan.correa@epfl.ch; anders.hagfeldt@epfl.ch

M. Anaya, Dr. G. Lozano, Dr. M. E. Calvo, Prof. H. Míguez
Institute of Materials Science of Seville
Spanish National Research Council-University of Seville
Av. Americo Vespucio 49, 41092 Seville, Spain
E-mail: h.miguez@csic.es

Dr. W. Tress, K. Domanski, Dr. M. Saliba, Dr. A. Abate, Prof. M. Grätzel
Laboratory of Photonics and Interfaces
Institute of Chemical Sciences and Engineering
École Polytechnique Fédérale de Lausanne
1015 Lausanne, Switzerland

T. Matsui
Research Division
Panasonic Corporation
1006 (Oaza Kadoma), Kadoma City, Osaka 571-8501, Japan

Dr. A. Abate
Adolphe Merkle Institute
University of Fribourg
Ch. du. Musée 3, CH-1700 Fribourg, Switzerland

DOI: 10.1002/adma.201600624

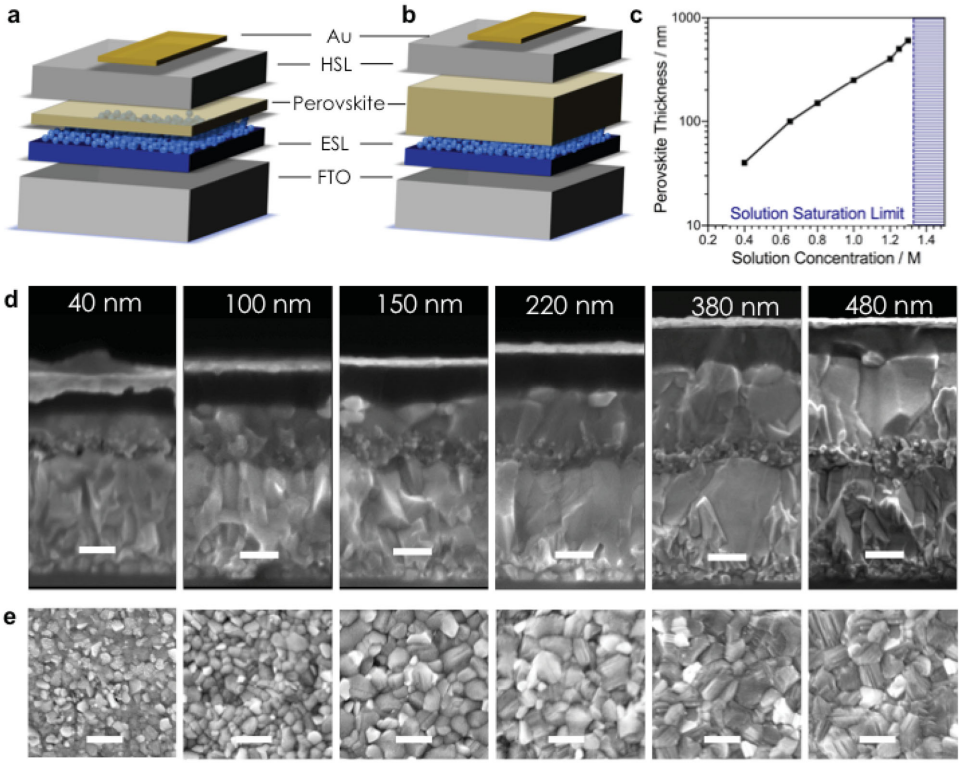

Figure 1. Solution concentration and its relation to crystal size/perovskite thickness of perovskite solar cells (PSC) studied in this work. a) Schematic of full PSCs with thin and b) thick perovskite layers. c) Perovskite capping layer thickness as a function of solution concentration (with respect to the Pb content). d) SEM images of cross-sectioned PSC devices; scale bar 200 nm. e) Top view of the bare perovskite film, scale bar 400 nm, for different perovskite film thicknesses.

whereas the conformal perovskite capping layer absorbs most of the light and transports the charges. The Spiro-OMeTAD is used as a hole selective layer (HSL). By varying the concentration of the perovskite solution and keeping the thickness of the thin mesoporous layer constant, we varied the thickness of the perovskite capping layer. Layers as thick as 600 nm deposited by spin coating were made from a solution concentration of 1.3 M, however, concentrations higher than 1.25 M lead to rapid formation of precipitates and inhomogeneous films. Figure 1c summarizes the change in perovskite thickness, as extracted from scanning electron micrographs (SEM), with respect to solution concentration. As clearly seen in the cross-sectional SEM images in Figure 1d, increasing the concentration from 0.4 M to 1.25 M yielded perovskite capping layers of about 40 and 480 nm, respectively, which sit atop the perovskite-filled mesoporous layer. Another effect associated with the thickness variation was observed for the crystal size in the capping layer. From the top view of the perovskite films as shown in Figure 1e, it is seen that the smallest crystals were about 40 nm and the largest ones about 400 nm, as the perovskite thickness was increased. We found that perovskite crystals for the thickest samples (380 and 480 nm) grow as a single grain from the top of the mesoporous ESL to the HSL (this metric will be used throughout the text), scaling with perovskite capping layer thickness. For samples with thinner layers, it is not very clear whether single crystals are sandwiched between the contacts or if there are a few crystals on top of each other. However, we can confidently say that only one or a few crystals are found in this dimension of the capping layer. We can therefore study both the optical properties and the electronic/ionic properties of small and large crystals by varying the thickness. No significant difference was found in the crystal structure of the perovskite films as shown by X-ray diffraction (Figure S2, Supporting Information).

Direct measurements of the spectral dependence of the fraction of light absorbed from full devices using different mixed perovskite capping layer thicknesses are displayed in **Figure 2**a. The absorptance onset for this mixed perovskite material is at ≈780 nm as previously reported.[14,15,22,23] The absorptance of the cells below 500 nm is close to 95% regardless of the perovskite layer thickness. This originates from the high values of the imaginary part of the complex refractive index of the perovskite (see Figure S3a, Supporting Information) and, to a lesser extent, from the parasitic absorption generated in the transparent conductive oxide layer and in the gold contact, especially for the thinnest devices. As a result, nearly all light transmitted through the substrate in the blue is absorbed within the PSC. In contrast, between ≈500 and 795 nm, where the extinction coefficient of the perovskite reduces, the fraction of the incident light absorbed by the cell increases with the perovskite thickness. Notice that an optimal behavior is found for a perovskite capping layer thickness of 480 nm for which the absorptance reaches values as high as 95% from ≈500 to 740 nm. The spectral dependence of the external quantum efficiency (EQE) of the devices is presented in Figure 2b. The area under each curve, which represents the number of carriers created by the device

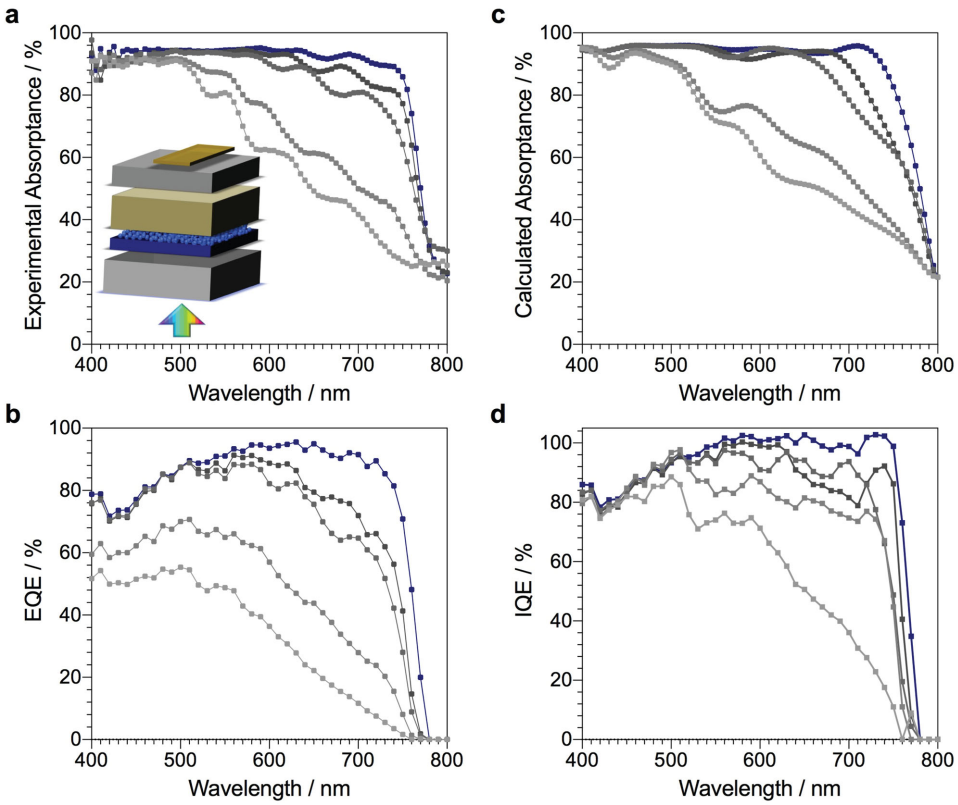

Figure 2. Optical properties of $FA_{0.83}MA_{0.17}(PbI_{0.83}Br_{0.17})_3$, films labeled here as "mixed," and spectral optical and electrical characterization of "mixed" perovskite based solar cells. a) Spectral dependence of the experimental absorptance. b) External quantum efficiency c) Calculated absorptance. d) Internal quantum efficiency of devices in which different "mixed" perovskite capping layer thicknesses have been deposited. Gray-to-black curves represent increment in thickness of the perovskite capping layer: 40, 150, 220, and 380 nm. Blue curve corresponds to the optimized case in which a 480 nm thick "mixed" perovskite capping layer is employed to maximize the device efficiency.

under solar illumination (J_{SC}), increases with the capping layer thickness (see **Table 1**), as it may be expected from the absorptance measurements. The extremely high optical quality of the layers comprising the devices enables the observation of spectral fringes arising from the interference between light reflected and transmitted in the different interfaces of the cell. Indeed, the EQE spectrum measured for each perovskite thickness features well-defined oscillations matching the ones noted in the absorptance curves. This resonant photocurrent generation has been previously reported for other third-generation solar cells,[24] demonstrating a precise control of the spectral response of the photovoltaic device.

In order to gain insight into the way these cells make use of the absorbed light, an optical model based on the transfer matrix formalism that considers all components depicted in Figure 1 (glass, FTO, TiO_2 compact layer, perovskite infiltrated

Table 1. Solar cell performance parameters for devices with different perovskite thickness at a scan rate of 10 mV s^{-1}. Short circuit photocurrent (J_{SC}), power conversion efficiency (PCE), open circuit voltage (V_{OC}), and fill factor (FF) as extracted from the data in Figure S4a (Supporting Information). The best six devices shown for concentrations varying from 0.4 to 1.25 M are from a single batch, whereas the last device is from a separate batch and measured under different light intensity. The latter uses antireflective tape yielding considerably higher currents (due to reduced glass reflection not accounted for in our model) around 24.4 mA cm^{-2} when normalized to 1 sun.

Perovskite concentration [M]	Capping layer thickness [nm]	V_{OC} [V]	J_{SC} [mA cm^{-2}]	FF [%]	PCE [%]	Light intensity [mW cm^{-2}]
0.40	40	0.93	11.2	51	5.29	98.6
0.65	100	1.11	15.5	59	10.2	98.6
0.80	150	1.12	20.0	73	16.7	98.6
1.00	220	1.12	21.0	76	18.0	98.6
1.20	380	1.11	21.9	76	18.8	98.6
1.25	480	1.12	22.9	76	19.7	98.6
1.25 (champion)	480	1.14	23.0	75	20.8	94.4

mesoporous TiO_2 layer, perovskite capping layer, Spiro-OMeTAD, and gold) was developed.[25] Our model, which does not account for crystal size variations, fairly reproduces the absorptance measured from the complete devices (see Figure 2c) and allows discriminating the fraction of light absorbed only by the perovskite (light harvesting efficiency, LHE) that is displayed in Figure S3 (Supporting Information). The internal quantum efficiency (IQE), estimated from the ratio of its EQE and LHE, is shown in Figure 2d for the different devices under analysis. For thick perovskite capping layers, the IQE is close to 100% from 500 to 770 nm, indicating that photogenerated carriers are collected with equal efficiency at both contacts. In contrast, IQE values diminish considerably as the thickness of the perovskite layer decreases. This feature is associated with the reduction of perovskite crystal size affecting the electric properties of the material, as it will be discussed below. On top of this, we observe a reduction in the IQE at shorter wavelengths (below 500 nm) that does not originate from a lower optical absorption. Consequently, such behavior should find an explanation in the efficiency of injection, transport, or collection of photogenerated carriers close to the ESL/perovskite interface where charges are predominantly generated by blue light.

We have already demonstrated that PSC absorptance is strongly dependent on the capping layer thickness. At the same time, quantum efficiency measurements evidence that perovskite crystal size has an influence on the electrical properties of the devices. In order to unveil the precise interplay between morphology and performance of PSCs an in-depth analysis of the fabricated devices is shown next. Photovoltaic characteristics of PSCs with different perovskite layers are presented in **Figure 3**. As seen in Figure 3a and Table 1, the champion device yielded a PCE of about 20.8% with a remarkably high V_{OC} of 1.14 V and a current density of 23 mA cm^{-2} (24.4 when normalized to 1 sun, using an antireflective coating) for a perovskite layer of 480 nm. As shown in Figure S4 and Table S1 (Supporting Information), an average PCE of 19%, V_{OC} of 1.12 V, current density J_{SC} of 22.3 mA cm^{-2}, and fill factor of 73% for 40 devices were obtained for devices with thick capping layers. By assuming a 100% charge collection efficiency we calculated the maximum J_{SC} that can be achieved by a device as a function of the perovskite capping layer thickness. Although our model accounts for the conductive glass and gold parasitic absorption and the reflection given by the air–glass interface, results shown in Figure 3b represent the ideal case in which every photon absorbed by the perovskite contributes to the photocurrent. The predicted J_{SC} for 480 nm devices is around 23 mA cm^{-2} according to our model of the full device, including losses due to glass reflection. However, applying an antireflective coating

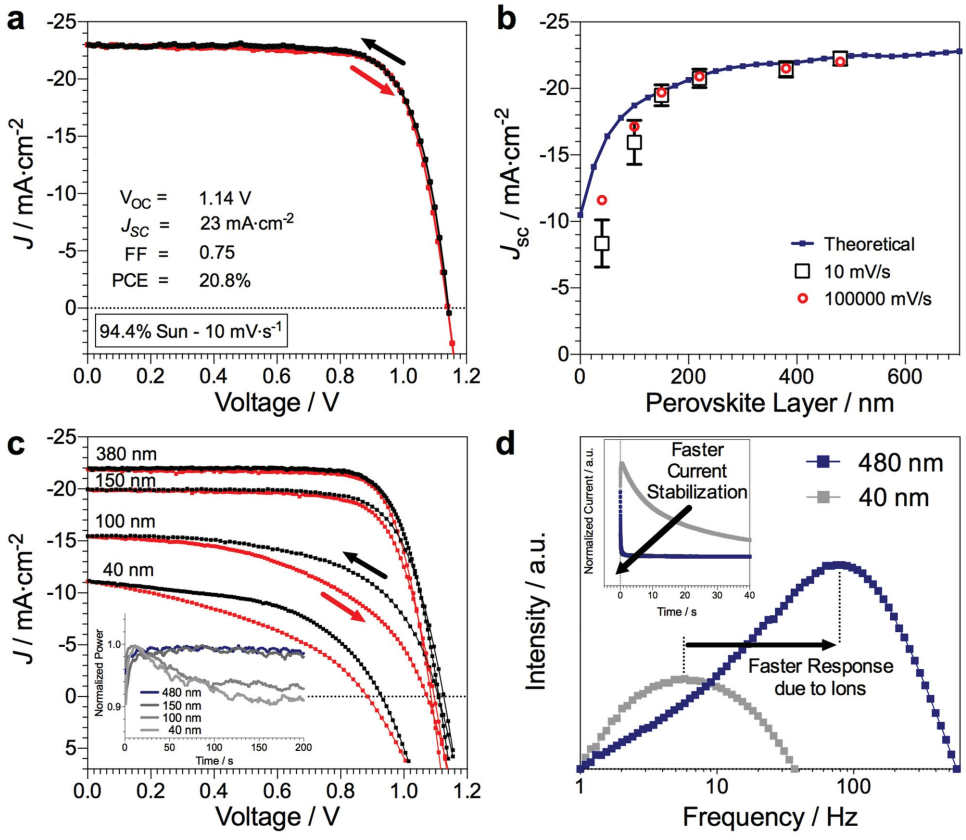

Figure 3. Current–voltage characteristics and physical properties of the mixed perovskite solar cells with varying capping layers. a) Backward and forward scans of a champion device. b) Calculated and experimental J_{SC} using an average value of at least six devices for scans at 10 mV s^{-1} and a single value of a *J–V* scan at 100 000 mV s^{-1} c) Backward and forward *J–V* scans accompanied by the normalized maximum power point tracking (inset). d) Intensity modulated photocurrent spectroscopy in the imaginary part of the current response in the low frequency range with current dynamics after prepolarization and switching to short-circuit current (inset) for selected devices.

increased the J_{SC} significantly as seen in our champion device in Figure 3a. Experimental results attained for thick capping layer-based devices are in very good agreement with the values expected from the model, which indicates that only for thicker devices all light harvested by the perovskite contributes to the current. Indeed, we demonstrate that our best performing devices follow the predicted maximum J_{SC} whereas those with thinner layers (40 and 100 nm) present more variability. The discrepancy between the calculated limits of the J_{SC} and the actual values measured for thin layers indicates that thinner layers with small crystals lead to charge collection efficiencies significantly lower than 100%. Figure S5 (Supporting Information) shows that devices with 40 and 100 nm layers do not saturate the current unless fast scan rates up to 100 000 mV s^{-1} are used, where currents match better those predicted by the model. This shows that thinner capping layers with smaller crystals are intrinsically limited by much less than 100% charge extraction, as shown in the IQE in Figure 2d.

Comparing the *J–V* data for the devices in Figure 3c and the statistics displayed in Figure S4c (Supporting Information), we observed that V_{OC} remains constant except for the thinnest device, where recombination is enhanced. This is in line with the work of Kim and Park, where no change in V_{OC} is seen for different crystal sizes.[20] The trend in fill factor is surprising, however: it increases monotonically with layer thickness and saturates at values of above 73% for capping layers larger than 150 nm (Figure S4e, Supporting Information). In general, the fill factor is either limited by "shunt" or "series" resistance effects. For *J–V* curves measured in the dark presented in Figure S6 (Supporting Information), we found high shunt resistances of more than 1 MOhm cm^{-2} (for the thinnest device more than 0.1 MOhm cm^{-2}), which do not influence the *J–V* curves under solar illumination. Consequently, the trend in FF is due to changes in the "series" resistance, whose values (approximated from a linear fit to the 1 sun *J–V* curves in forward bias and summarized in Figure S6, Supporting Information) are < 7.5, < 6, 5.2, 4.8, and 3.7 Ohm cm^{-2} for PSCs with capping layers of 40, 100, 150, 220, and 380 nm, respectively. As the variable parameter here is the perovskite layer thickness, which in turn modifies the crystal size, the reduced FF is attributed to a modified charge carrier collection efficiency as a function of voltage. In this case, a decrease of FF with the layer thickness is expected as long as the properties of the layer remain unaffected by the crystal dimensions. The large modification in FF, and fairly unchanged V_{OC} (except in the thinnest devices), with respect to crystal size, indicates that crystal size is determining the charge collection properties without modifying recombination in perovskite devices.

As shown in Figure 3c (and expanded in Figure S8, Supporting Information), devices with the capping layers thicker than 150 nm showed very low hysteresis. The hysteresis becomes stronger and affects the FF of the forward scan for the thin (40 and 100 nm) devices. Similar trends have been shown by Kim and Park.[20] This is expected as the charge collection (see Figure 2) is problematic in these devices and it strongly depends on the voltage applied. This series demonstrates that the microscopic reason for the hysteresis has to be distinguished from the occurrence of the hysteresis. The former seems inherent to perovskite, whereas the latter depends on whether charge carrier collection is sufficiently low, so that the fill factor can suffer from a reduced field in the device. Tracking of the maximum power point of select devices is presented as an inset in Figure 3c, corroborating our findings on hysteresis. Samples with 40 and 100 nm crystallites show a slow stabilization at ≈92% of the original power output, whereas samples with 150 nm or larger crystals show stabilized currents with no significant transients.

For perovskite solar cells hysteresis in the *J–V* curve has been reported and explained by ionic movement modifying the electric field within the perovskite layer, which in turn can affect charge carrier collection efficiency and recombination behavior.[21] Therefore, it is important to understand the role of ionic movement in devices with different morphological characteristics. Figure 3d presents the Bode imaginary plot of the current response to the intensity modulated photocurrent (IMPS) of devices with the smallest and the largest crystals. The dataset was obtained from Figure S9 (Supporting Information) where the whole frequency range shows three main peaks in the imaginary part of the current response. The measurement clearly shows that the slow component in the 1–100 Hz range is present for all devices. We attribute this to a response to light modulation which is due to ionic movement within the perovskite and it is in good agreement with recent studies where impedance spectroscopy is used to identify this component as ionic transport.[26]

To further understand this slow time constant we used temperature dependent IMPS measurements as shown in Figure S10 (Supporting Information). Here we found that devices with large crystals exposed to temperatures close to 0 °C have much slower response time than those at room temperature, whereas the response is much faster at higher temperatures. This further confirms that the slow component is not an electronic transport time constant, but describes a response due ionic movement, which is a thermally activated transport mechanism.

Interestingly, the timescale of this ion-induced low frequency component is very different for different crystal size devices. Larger crystals showed prominent peaks at very fast time scales, whereas smaller crystals showed an order of magnitude slower behavior (for the full range of crystal size see Figure S9b, Supporting Information), from about 10 to over 160 ms, respectively. This can be correlated to the hysteresis behavior: the larger the crystals, the faster the response due to ionic movement in the IMPS measurement. Consequently, transients at each voltage step in the *J–V* curve are much faster allowing for 10 mV s^{-1} scan rates to yield nearly hysteresis-free conditions. On the other hand, slower response for the small crystal devices leads to slower reorganization of the ions during reverse and forward bias sweeps. This leads to slower stabilization of currents in the device during operating conditions and therefore showing increased hysteresis in the *J–V* curve, even at slow scan speeds.

To elucidate on this subject we obtained current transient decays for devices from small to large crystals, by switching from V_{OC} to J_{SC} as shown in the inset of Figure 3d (full details can be found in Figure S11, Supporting Information). The current transients indicate the time scale required for ionic stabilization, as shown by some of us in recent reports.[21,27]

In agreement with the IMPS findings, the smallest crystal device shows the slowest transient (Figure S11a,b, Supporting Information), whereas those with thicker layers (Figure S11c, Supporting Information) exhibit very fast current stabilization. These measurements corroborate the IMPS findings on response timescales for different crystal sizes.

We studied the hysteresis behavior with respect to capping layer thickness and we measured PSCs with 40, 150, and 480 nm thick layers at the same scan rate but at different temperatures as presented in Figure S12 (Supporting Information). For all devices, decreasing the temperature to −20 °C yielded highly hysteretic *J*–*V* curves. Hysteresis remained large at 0 °C, and almost disappeared at room temperature, except for the thinnest devices with the smallest crystals, where hysteresis and low fill factor prevailed. Increasing the temperature to 40 °C improved the fill factor of the thinnest device (Figure S12d, Supporting Information) and reduced further the hysteresis of the thickest device (Figure S12d, Supporting Information). We attribute this to faster stabilization of the currents due to thermal activation of ionic displacement for thicker, large-crystal devices, which is necessary for obtaining steady-state photovoltaic parameters at intermediate scan rates.

In addition to slower ionic transients, the thinnest devices are intrinsically influenced by the increased series resistance presumably due to the large number of grain boundaries, as explained above. This can also be explained by an increase of surface deffects with increased surface area in small crystallites, where ion vacancies play a bigger role. These effects associated with small perovskite crystallites are responsible for the inferior photovoltaic parameters shown in Figure 3c. Therefore, large crystals showing fast ionic transient behavior and improved series resistance are essential for obtaining hysteresis-free high efficiency PSCs.

PSCs with different perovskite capping layer thicknesses, and crystals sizes therein, were studied and rigorously connected to both the electro-optical properties and ionic movement. The optimized device configuration with a champion PCE of 20.8% was achieved with a perovskite-infiltrated thin mesoporous TiO_2 layer and a 480 nm thick capping layer composed of large crystals. We simulated the optical properties of the perovskite material to show that the optimal thickness yields a J_{SC} maximum of 23 mA cm^{-2}. Furthermore, high fill factor and low hysteresis results from perovskite capping layers with a thickness of at least 150 nm that show larger crystals and reduced number of grain boundaries. It is explained by the favorable ionic transient behavior, and improved series resistance associated with thicker capping layers that are composed of large crystals. Our work then shows the importance of morphological features, such as crystal size and the perovskite layer thickness in PSCs to achieve over 20% power conversion efficiencies.

Experimental Section

Electron Selective Layer Preparation: Nippon sheet glass 10 Ω sq^{-1} was cleaned by sonication in 2% Hellmanex water solution for 30 min. After rinsing with deionized water and ethanol, the substrates were further cleaned with UV ozone treatment for 15 min. Then, 50–70 nm TiO_2 compact layer was deposited on FTO via spray pyrolysis at 450 °C from a precursor solution of titanium diisopropoxide bis(acetylacetonate) in anhydrous ethanol. After the spraying, the substrates were left at 450 °C for 45 min and left to cool down to room temperature. Then, mesoporous TiO_2 layer was deposited by spin coating for 20 s at 4000 rpm with a ramp of 2000 rpm s^{-1}, using 30 nm particle paste (Dyesol 30 NR-D) diluted in ethanol to achieve 150–200 nm thick layer. After the spin coating, the substrates were immediately dried at 100 °C for 10 min and then sintered again at 450 °C for 30 min under dry air flow.

Li-doping of mesoporous TiO_2 was accomplished by spin coating a 0.1 M solution of Li-TFSI in acetonitrile. The solution is prepared freshly before the application in nitrogen atmosphere. 50 µL was poured on 1.4 × 2.4 cm^2 substrate. Li$^+$-treated electrodes were completed with a second calcination step at 450 °C for 30 min. After cooling down to 150 °C the substrates were immediately transferred in a nitrogen atmosphere glove box for depositing the perovskite films.

Perovskite Precursor Solution and Film Preparation: The perovskite films were deposited from a precursor solution containing FAI (1 M), PbI_2 (1.1 M, TCI Chemicals), MABr (0.2 M), and $PbBr_2$ (0.2 M, Alfa Aesar) in anhydrous DMF:DMSO 4:1 (v:v, Acros). The perovskite solution was spin-coated in a two-step program; first at 1000 for 10 s and then at 6000 rpm for 30 s. During the second step, 100 µL of chlorobenzene was poured on the spinning substrate 15 s prior the end of the program. The substrates were then annealed at 100 °C for 1 h in a nitrogen filled glove box.

The spiro-OMeTAD (Merck) solution (70 × 10^{-3} M in chlorobenzene) was spun at 4000 rpm for 20 s. The spiro-OMeTAD was doped at a molar ratio of 0.5, 0.03, and 3.3 with bis(trifluoromethylsulfonyl)imide lithium salt (Li-TFSI, Sigma Aldrich), tris(2-(1H-pyrazol-1-yl)-4-tert-butylpyridine)-cobalt(III) tris(bis(trifluoromethylsulfonyl)imide) (FK209, Dyenamo), and 4-tert-Butylpyridine (Sigma Aldrich), respectively.[28–30] As the last step 70–80 nm of gold top electrode was thermally evaporated under high vacuum. Silver paste (Sigma) was used on the Au contact pads in order to improve electrical connection between samples and contact pins of our measurement setup (an image of the samples is seen in Figure S1, Supporting Information).

Solar Cell and Material Characterization: A ZEISS Merlin high resolution scanning electron microscopy (HR-SEM) was used to characterize the morphology of the device cross-section. The solar cells were measured using a 450 W xenon light source (Oriel). The spectral mismatch between AM 1.5G and the simulated illumination was reduced by the use of a Schott K113 Tempax filter (Präzisions Glas & Optik GmbH). The light intensity was calibrated with a Si photodiode equipped with an IR-cutoff filter (KG3, Schott) and it was recorded during each measurement. Current–voltage characteristics of the cells were obtained by applying an external voltage bias while measuring the current response with a digital source meter (Keithley 2400). The voltage scan rate was 10 mV s^{-1} and no device preconditioning was applied before starting the measurement, such as light soaking or forward voltage bias applied for a long time. The starting voltage was determined as the potential at which the cells furnished 1 mA in forward bias, no equilibration time was used. The cells were masked with a black metal mask limiting the active area to 0.16 cm^2 and reducing the influence of the scattered light.

Autolab potentiostat PGSTAT30 driven by NOVA software: Using a red LED, light intensity was modulated while short-circuit current variation was recorded. Device temperature was controlled by a home built peltier and temperature controller for the temperature-dependence experiments.

The samples were analyzed by x-ray diffraction using a Bruker D8 Advance X-ray diffractometer using Cu Kα radiation (λ = 0.154178 nm) at a scanning rate of 0.02° s^{-1} in the 2θ range from 20° to 60°.

Optical Characterization and Modeling: In order to obtain absorptance spectra of the PSCs, a setup in which white light (Ocean Optics, HL-2000) is directed to enter an integrating sphere (Labsphere, 10 inch) was used. A fiber-coupled spectrophotometer (Ocean Optics, USB 2000+), which is connected to a computer, was employed to acquire the spectra.

A home-made setup comprising a monochromator with a 1140 g mm^{-1} grating (Mcpherson 272) attached to a 300 W xenon lamp, controlled

by a digital scan drive system (McPherson 789A-3) and a picoammeter (Keithley 6485), was used in order to obtain the spectral dependence of the external quantum efficiency of the different perovskite-based devices. Second-order harmonics produced by the monochromator were removed by using a short pass filter with a cutoff wavelength of 400 nm. With the aim of getting absolute values, a calibrated silicon photodiode (D8-Si-100 TO-8 detector, Sphere Optics) was employed to correct the measurements. An optical model based on the transfer matrix formalism was developed, which allowed calculating the electric field intensity within the layered structure and, thus, estimating the fraction of the incident light absorbed by each material comprising the perovskite device. Full details on the model can be found elsewhere, as well as evidence of its suitability to describe the optics of PSCs.[25] For the calculation of maximum J_{sc}, EQE = LHE was assumed. Consequently, collection and injection efficiencies were considered to be 100%. In this way, such calculations render an upper limit for the values of J_{sc}, the ideal situation when each photon absorbed by the perovskite contributes to the photocurrent.

Supporting Information

Supporting Information is available from the Wiley Online Library or from the author.

Acknowledgements

J.P.C.B. and M.A. contributed equally to this work. The authors thank Dr. Fabrizio Giordano and Jiyoun Seo for their help in the development of the original perovskite recipe, and Norman Pellet for discussions. The research leading to these results received funding from the European Research Council under the European Union's Seventh Framework Programme (FP7/2007-2013)/ERC grant agreement No. 307081 (POLIGHT) Project, the Spanish Ministry of Economy and Competitiveness under Grant MAT2014-54852-R. M.A. is grateful to "La Caixa" Foundation for its financial support. A.A. received funding from the European Union's Seventh Framework Programme for research, technological development, and demonstration under grant agreement No. 291771.

Received: February 1, 2016
Revised: March 1, 2016
Published online: April 28, 2016

[1] A. Kojima, K. Teshima, Y. Shirai, T. Miyasaka, *J. Am. Chem. Soc.* **2009**, *131*, 6050.
[2] NREL : National Center For Photovoltaics Home Page, www.nrel.gov/ncpv. Accessed: 20 January, **2016**.
[3] N. Pellet, P. Gao, G. Gregori, T. Y. Yang, M. K. Nazeeruddin, J. Maier, M. Grätzel, *Angew. Chem. Int. Ed.* **2014**, *53*, 3151.
[4] C. C. Stoumpos, C. D. Malliakas, M. G. Kanatzidis, *Inorg. Chem.* **2013**, *52*, 9019.
[5] M. M. Lee, J. Teuscher, T. Miyasaka, T. N. Murakami, H. J. Snaith, *Science* **2012**, *338*, 643.
[6] J. Burschka, N. Pellet, S.-J. Moon, R. Humphry-Baker, P. Gao, M. K. Nazeeruddin, M. Grätzel, *Nature* **2013**, *499*, 316.
[7] Z. Xiao, C. Bi, Y. Shao, Q. Dong, Q. Wang, Y. Yuan, C. Wang, Y. Gao, J. Huang, *Energy Environ. Sci.* **2014**, *7*, 2619.
[8] M. Liu, M. B. Johnston, H. J. Snaith, *Nature* **2013**, *501*, 395.
[9] O. Malinkiewicz, A. Yella, Y. H. Lee, G. M. Espallargas, M. Graetzel, M. K. Nazeeruddin, H. J. Bolink, *Nat. Photonics* **2014**, *8*, 128.
[10] G. Xing, N. Mathews, S. Sun, S. S. Lim, Y. M. Lam, M. Grätzel, S. Mhaisalkar, T. C. Sum, *Science* **2013**, *342*, 344.
[11] S. D. Stranks, G. E. Eperon, G. Grancini, C. Menelaou, M. J. Alcocer, T. Leijtens, L. M. Herz, A. Petrozza, H. J. Snaith, *Science* **2013**, *342*, 341.
[12] W. Tress, N. Marinova, O. Inganäs, M. K. Nazeeruddin, S. M. Zakeeruddin, M. Graetzel, *Adv. Energy Mater.* **2015**, *5*, 1400812.
[13] W. S. Yang, J. H. Noh, N. J. Jeon, Y. C. Kim, S. Ryu, J. Seo, S. I. Seok, *Science* **2015**, *348*, 1234.
[14] N. J. Jeon, J. H. Noh, W. S. Yang, Y. C. Kim, S. Ryu, J. Seo, S. I. Seok, *Nature* **2015**, *517*, 476.
[15] D. Bi, W. Tress, M. I. Dar, P. Gao, J. Luo, C. m. Renevier, K. Schenk, A. Abate, F. Giordano, J. P. Correa Baena, J.-D. Decoppet, S. M. Zakeeruddin, M. K. Nazeeruddin, M. Grätzel, A. Hagfeldt, *Sci. Adv.* **2016**, *2*, e1501170.
[16] C. Momblona, O. Malinkiewicz, C. Roldán-Carmona, A. Soriano, L. Gil-Escrig, E. Bandiello, M. Scheepers, E. Edri, H. J. Bolink, *APL Mater.* **2014**, *2*, 081504.
[17] C. Roldan-Carmona, O. Malinkiewicz, R. Betancur, G. Longo, C. Momblona, F. Jaramillo, L. Camacho, H. J. Bolink, *Energy Environ. Sci.* **2014**, *7*, 2968.
[18] V. D'Innocenzo, G. Grancini, M. J. P. Alcocer, A. R. S. Kandada, S. D. Stranks, M. M. Lee, G. Lanzani, H. J. Snaith, A. Petrozza, *Nat. Commun.* **2014**, *5*.
[19] G. Grancini, A. R. Srimath Kandada, J. M. Frost, A. J. Barker, M. De Bastiani, M. Gandini, S. Marras, G. Lanzani, A. Walsh, A. Petrozza, *Nat. Photonics* **2015**, *9*, 695.
[20] H.-S. Kim, N.-G. Park, *J. Phys. Chem. Lett.* **2014**, *5*, 2927.
[21] W. Tress, N. Marinova, T. Moehl, S. M. Zakeeruddin, M. K. Nazeeruddin, M. Gratzel, *Energy Environ. Sci.* **2015**, *8*, 995.
[22] M. Saliba, S. Orlandi, T. Matsui, S. Aghazada, M. Cavazzini, J.-P. Correa-Baena, P. Gao, R. Scopelliti, E. Mosconi, K.-H. Dahmen, F. De Angelis, A. Abate, A. Hagfeldt, G. Pozzi, M. Graetzel, M. K. Nazeeruddin, *Nat. Energy* **2016**, *1*, 15017.
[23] F. Giordano, A. Abate, J. P. Correa Baena, M. Saliba, T. Matsui, S. Im, A. Hagfeldt, M. K. Nazeeruddin, M. Graetzel, *Nat. Commun.* **2016**, *7*, 10379.
[24] M. Anaya, M. E. Calvo, J. M. Luque-Raigón, H. Míguez, *J. Am. Chem. Soc.* **2013**, *135*, 7803.
[25] M. Anaya, G. Lozano, M. E. Calvo, W. Zhang, M. B. Johnston, H. J. Snaith, H. Míguez, *J. Phys. Chem. Lett.* **2015**, *6*, 48.
[26] M. Bag, L. A. Renna, R. Y. Adhikari, S. Karak, F. Liu, P. M. Lahti, T. P. Russell, M. T. Tuominen, D. Venkataraman, *J. Am. Chem. Soc.* **2015**, *137*, 13130.
[27] K. Domanski, W. Tress, T. Moehl, M. Saliba, M. K. Nazeeruddin, M. Grätzel, *Adv. Funct. Mater.* **2015**, *25*, 6936.
[28] A. Abate, T. Leijtens, S. Pathak, J. Teuscher, R. Avolio, M. E. Errico, J. Kirkpatrik, J. M. Ball, P. Docampo, I. McPherson, H. J. Snaith, *Phys. Chem. Chem. Phys.* **2013**, *15*, 2572.
[29] A. Abate, D. R. Staff, D. J. Hollman, H. J. Snaith, A. B. Walker, *Phys. Chem. Chem. Phys.* **2014**, *16*, 1132.
[30] H. J. Snaith, A. Abate, J. M. Ball, G. E. Eperon, T. Leijtens, N. K. Noel, S. D. Stranks, J. T.-W. Wang, K. Wojciechowski, W. Zhang, *J. Phys. Chem. Lett.* **2014**, *5*, 1511.